Editors' Suggestion   Featured in Physics

Breakdown of Emergent Chiral Order and Defect Chaos in Nonreciprocal Flocks

Charlotte Myin,[1,*] Suropriya Saha,[1,†] and Benoît Mahault[2,1,‡]
[1]*Max Planck Institute for Dynamics and Self-Organization (MPI-DS), 37077 Göttingen, Germany*
[2]*Laboratoire Charles Coulomb (L2C), UMR 5221 CNRS–Université de Montpellier, Montpellier F-34095, France*

(Received 4 May 2026; accepted 16 June 2026; published 8 September 2026)

We show that chiral order in two-dimensional nonreciprocal flocking mixtures is generically unstable. Combining large-scale agent-based simulations with a coarse-grained continuum description, we demonstrate that rotating chiral states emerging from antisymmetric couplings are destroyed by the proliferation of topological defects. The resulting dynamics is spatiotemporally chaotic and characterized by a finite correlation length that diverges as nonreciprocity vanishes. On length scales below this cutoff, density and orientational order fluctuations remain scale-free, but the associated scaling exhibits nonuniversal exponents. We attribute this atypical behavior to the coupling between density and order, which causes topological defects to act as persistent sources of nonlinear fluctuations.

DOI: 10.1103/c6dy-38z1

A central question in condensed matter physics is whether emergent order can persist at macroscopic scales. At equilibrium, the breaking of a continuous symmetry produces massless Goldstone modes whose fluctuations, as formalized by the Hohenberg-Mermin-Wagner theorem, destroy long-range order in dimensions $d \leq 2$ [1,2]. Systems driven far from equilibrium such as active matter can circumvent this constraint. Assemblies of coherently moving agents, or flocks, exhibit true long-range polar order in $d \geq 2$ [3–10] and are a paradigmatic, but not unique [11–17], example. Although robust to smooth, long-wavelength fluctuations, polar order in flocks has recently been shown to be particularly vulnerable to rare but large fluctuations inducing nucleation of counterpropagating fronts. The flocking phase can then become partially [18] or entirely [15,19–22] metastable.

Nonreciprocal mixtures—which can be described in terms of effective interactions breaking action-reaction symmetry—constitute another particularly rich class of active matter [23,24]. One of their hallmarks is the emergence of oscillatory instabilities arising through the crossing of an exceptional point [25–27]. For systems subject to conservation laws, these instabilities give rise to a variety of dynamical patterns [25,26,28–36], whereas nonconserved dynamics displays global oscillations and persistent rotations [27,37–48].

In multispecies flocks with nonreciprocal interactions, global rotations of the order parameter are associated with the spontaneous breaking of both chiral and time-translation symmetries. General arguments suggest that the associated Goldstone mode obeys a compact Kardar-Parisi-Zhang (KPZ) equation [16,49–53]. A major consequence is that, since KPZ interfaces are rough in all dimensions $d \leq 2$ [49,54], fluctuations of the Goldstone mode suppress true long-range chiral order. More dramatically, in $d \leq 2$ compact KPZ dynamics allows for the proliferation of topological defects that preclude any long-range correlations [44,45,55], while scale-free behavior should persist only below a cutoff scale set by the mean interdefect separation [53,56]. These arguments, however, do not account for the fact that nonreciprocal flocks are also characterized by several conserved density fields [27,52,57–59]. How the inherent coupling between density and polarity affects the stability of order and scaling properties in such active nonreciprocal mixtures remains so far unexplored.

In this Letter, we investigate the robustness of spontaneously emerging global chiral order in nonreciprocal flocks. Combining large-scale agent-based simulations with a coarse-grained continuum theory, our results confirm that chiral order and long-range correlations are generically destroyed by the proliferation of topological defects. The resulting highly dynamical defect-chaos phase is dominated by strong spatiotemporal fluctuations, where both orientational and density correlations exhibit scale-free behavior over intermediate length scales. Remarkably, the associated scaling exponents are nonuniversal and incompatible with those of the KPZ universality class. We attribute these anomalous scaling properties to the

[*]Contact author: charlotte.myin@ds.mpg.de
[†]Contact author: suropriya.saha@ds.mpg.de
[‡]Contact author: benoit.mahault@umontpellier.fr

coupling between density and orientational order, by which topological defects act as nucleation sites for highly nonlinear perturbations that constantly remodel both density and polarity landscapes.

Minimal model for nonreciprocal flocks—We consider a binary mixture of Vicsek-like particles [3,57] moving at constant speed on a two-dimensional plane. Particles align their velocities with neighbors located within a unit-radius disk, in the presence of angular noise. The two species are labeled A and B. A particle k of species S is characterized at discrete time t by its position $\boldsymbol{r}_k^{\mathrm{S}}(t)$ and its self-propulsion orientation $\theta_k^{\mathrm{S}}(t)$, which evolve according to

$$\boldsymbol{r}_k^{\mathrm{S}}(t+1) = \boldsymbol{r}_k^{\mathrm{S}}(t) + v_0 \hat{\boldsymbol{u}}[\theta_k^{\mathrm{S}}(t+1)], \tag{1a}$$

$$\theta_k^{\mathrm{S}}(t+1) = \arg\left[\sum_{\mathrm{U},j} \chi^{\mathrm{SU}} e^{i\theta_j^{\mathrm{U}}(t)} + \eta n_k(t) e^{i\xi_k(t)}\right], \tag{1b}$$

where $\hat{\boldsymbol{u}}[\theta] = (\cos\theta \sin\theta)^T$, v_0 is the self-propulsion speed and η the noise strength, which are taken identical for both species. The sum in Eq. (1) runs over all $n_k(t)$ neighbors j of species $\mathrm{U} = \mathrm{A}, \mathrm{B}$.

The aligning interactions are encoded in the matrix χ^{SU}. For $\chi^{\mathrm{SU}} > 0$, particles of species S align their direction of motion with that of particles of species U, while for $\chi^{\mathrm{SU}} < 0$ they anti-align. Throughout this work, we set $\chi^{\mathrm{AA}} = \chi^{\mathrm{BB}} = 1$. We define $\bar{\chi} = \frac{1}{2}(\chi^{\mathrm{AB}} + \chi^{\mathrm{BA}})$, which quantifies the net tendency for alignment ($\bar{\chi} > 0$) or anti-alignment ($\bar{\chi} < 0$), as well as $\Delta\chi = \frac{1}{2}(\chi^{\mathrm{AB}} - \chi^{\mathrm{BA}})$, which measures the degree of nonreciprocity. Interactions are reciprocal when $\Delta\chi = 0$, and nonreciprocal otherwise.

The phase diagram of the model (1) in the weakly nonreciprocal regime $|\bar{\chi}| > |\Delta\chi|$ has been characterized in Ref. [57]. In this case, the two species mutually align or anti-align, albeit with different strengths, and typically self-organize into various homogeneous phases or spatial patterns that are globally polar, antipolar, or disordered. Hereafter, we instead focus on the strongly nonreciprocal regime, $|\Delta\chi| > |\bar{\chi}|$, where one species aligns with the other while the latter simultaneously anti-aligns. This antagonistic coupling induces dynamical frustration, which underlies the emergence of rotating phases spontaneously breaking chiral and time-translation symmetries [27].

From now on, we fix $v_0 = 1$ and focus on the case $\bar{\chi} = 0$ (see Supplemental Material [60] for additional data at $\bar{\chi} \neq 0$, leading to qualitatively similar results). Equation (1) are simulated in periodic square domains of linear size L with equal number densities $\rho^{\mathrm{A,B}} = \rho_0 = \frac{1}{2}$. Using the fact that this setting is symmetric upon exchanging $\mathrm{A} \leftrightarrow \mathrm{B}$ and the sign of $\Delta\chi$, we further restrict our analysis to $\Delta\chi > 0$, so that $\chi^{\mathrm{AB}} > 0$ and $\chi^{\mathrm{BA}} < 0$.

A phase diagram in the noise-nonreciprocity plane is shown in Fig. 1(a) for systems of size $L = 512$. On the $\Delta\chi = 0$ line, the two species do not interact and each

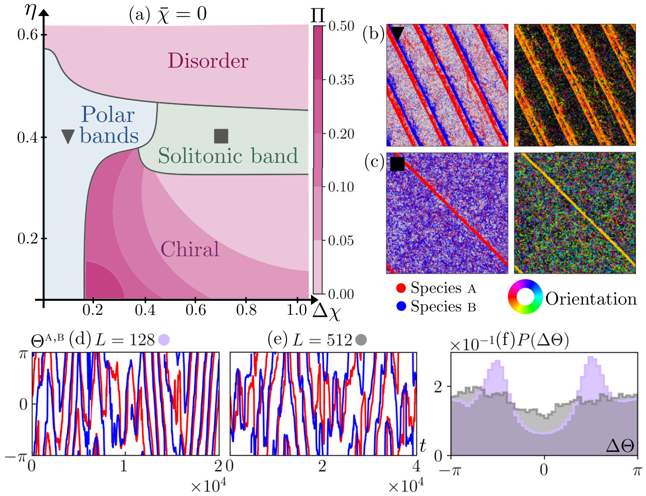

FIG. 1. Phase behavior of nonreciprocal flocks in the strong nonreciprocity regime. (a) Schematic phase diagram in the $(\Delta\chi, \eta)$ plane with $L = 512$. The "chiral" region is colored according to the global polarity averaged over species $\Pi = \frac{1}{2}(\Pi^{\mathrm{A}} + \Pi^{\mathrm{B}})$. See Ref. [60] for additional details on the labeling of the phases. (b),(c) Representative snapshots of the parallel bands (b) and solitonic band (c) phases. Particles are coloured according to species (orientation) in the left (right) panel (caption below), the corresponding points in (a) are indicated with solid symbols. (d),(e) Time series of the global polarity orientations $\Theta^{\mathrm{A,B}}$ for $\Delta\chi = 0.2$ and $\eta = 0.2$ with $L = 128$ (d) and 512(e). The red(blue) curves correspond to species A(B). (f) Corresponding probability distributions of $\Delta\Theta = \Theta^{\mathrm{B}} - \Theta^{\mathrm{A}}$ for $L = 128$ (purple) and 512 (gray).

behaves as an independent flock, undergoing a liquid-gas-like transition to collective motion as the noise η is decreased [58]. As for single-species flocks, the coexistence phase consists of a periodic array of dense, ordered bands propagating in a dilute, disordered background. For small $\Delta\chi > 0$, the species primarily self-organize into spatially synchronized arrangements of traveling bands [62], as shown in Fig. 1(b). In each pair of bands, the aligning species (here A) resides at the front, and the anti-aligning species (B) at the back. As discussed in Refs. [46,47,57], a similar synchronization mechanism occurs for mutually aligning species and arises from the nonreciprocal nature of the interactions.

For larger values of $\Delta\chi$, the high-noise disordered phase is bordered by a new phase [green region in Fig. 1(a)] in which species A forms a localized solitonic band propagating through a globally disordered gas, as displayed in Fig. 1(c). When initializing simulations with multiple bands, for instance, by duplicating an existing configuration, these structures rapidly merge, indicating that this state should always consist of a single band [see Supplemental Material movie (SMov) 1 [60]]. For sufficiently large $\Delta\chi$, this band typically reaches densities $\gg \rho_0$, such that it remains remarkably stable even when $\Delta\chi \to 1$ where $\chi^{\mathrm{AA}} \simeq \chi^{\mathrm{AB}}$, despite A particles continuously interacting with a disordered bath of B particles. A more detailed investigation of this structure will be presented elsewhere.

Further decreasing the noise, the system enters a homogeneous phase in which chiral and time-translation symmetries are spontaneously broken. In sufficiently small systems and for weak nonreciprocity, the orientations $\Theta^{\mathrm{S}}(t)$ of both species global polar order, $\mathbf{\Pi}^{\mathrm{S}} = \langle \hat{\boldsymbol{u}}[\theta_k^{\mathrm{S}}] \rangle_k = \Pi^{\mathrm{S}} \hat{\boldsymbol{u}}(\Theta^{\mathrm{S}})$, exhibit persistent rotations with a well-defined angular frequency, as reported in Fig. 1(d) and SMov 2 in [60]. This chiral rotation corresponds to a chasing dynamics of the global polarities, which maintain a finite phase shift $\Delta\Theta = \Theta^{\mathrm{B}} - \Theta^{\mathrm{A}}$. Rotations are occasionally interrupted by reversals, such that clockwise and counterclockwise rotations occur with equal probability, as evidenced by the bimodality of the distribution $P(\Delta\Theta)$ shown in Fig. 1(f).

However, increasing the system size leads to a rapid deterioration of global order. Reversal events become increasingly frequent [Fig. 1(e)], leading to the progressive flattening of $P(\Delta\Theta)$, while the global polarities Π^{S} decay rapidly as L increases [Fig. 2(a)]. As a result, the noise-dependent threshold value of $\Delta\chi$ below which global order is perceptible becomes lower in larger systems. For sufficiently small $\Delta\chi$, the homogeneous chiral phase is also metastable to the nucleation of polar bands. The characteristic nucleation time, however, increases rapidly with system size. In sufficiently large systems, a homogeneous chiral phase can thus be stabilized for several millions time steps even for values of $\Delta\chi$ lower than those indicated by the boundary with polar bands in Fig. 1(a).

Breakdown of chiral order and defect-chaos phase—Increasing system size, the chiral phase gradually becomes populated by topological defects [Fig. 2(h) and SMov 3 [60]]. The presence of these defects induces a finite correlation length, which is responsible for the rapid decay of the global polar order with increasing system size. We measured this correlation length by computing the coarse-grained density $\rho^{\mathrm{S}}(\boldsymbol{r},t) = \sum_k \delta(\boldsymbol{r} - \boldsymbol{r}_k^{\mathrm{S}}(t))$ and polarity $\boldsymbol{p}^{\mathrm{S}}(\boldsymbol{r},t) = \rho^{\mathrm{S}}(\boldsymbol{r},t)^{-1} \sum_k \hat{\boldsymbol{u}}[\theta_k^{\mathrm{S}}(t)] \delta(\boldsymbol{r} - \boldsymbol{r}_k^{\mathrm{S}}(t))$ fields. In Fourier space, the equal-time two-point correlation functions of both density fluctuations $\rho^{\mathrm{S}}(\boldsymbol{r},t) - \rho_0$ and polarity exhibit a plateau at small wave number q, as shown in Figs. 2(b) and 2(c) for species A (see Fig. 4 in End Matter for analogous results for B). Defining the density and polarity correlation lengths, ξ_ρ and ξ_p, from the half-width at half maximum of the $q = 0$ peak, we show in Fig. 2(d) that both ξ_ρ and ξ_p grow upon reducing $\Delta\chi$, with a trend compatible with $\xi_{\rho,p} \sim \Delta\chi^{-2}$.

For weak nonreciprocity, ξ_p becomes sufficiently large to unveil an apparent algebraic decay of the polarity correlation function over an intermediate range of wave numbers [Fig. 2(b)]. Remarkably, the associated exponents appear to vary with $\Delta\chi$. This can be seen most clearly by examining the local exponent of the correlation function $C_p(q)$, defined as $\sigma_p = -\mathrm{d}\ln C_p / \mathrm{d}\ln q$, which grows from zero and reaches a plateau σ_p^* at intermediate wave numbers, corresponding to a local power law decay $C_p(q) \simeq q^{-\sigma_p^*}$. As shown in Fig. 2(e), σ_p^* increases systematically as $\Delta\chi$ decreases and ξ_p grows, while it does not

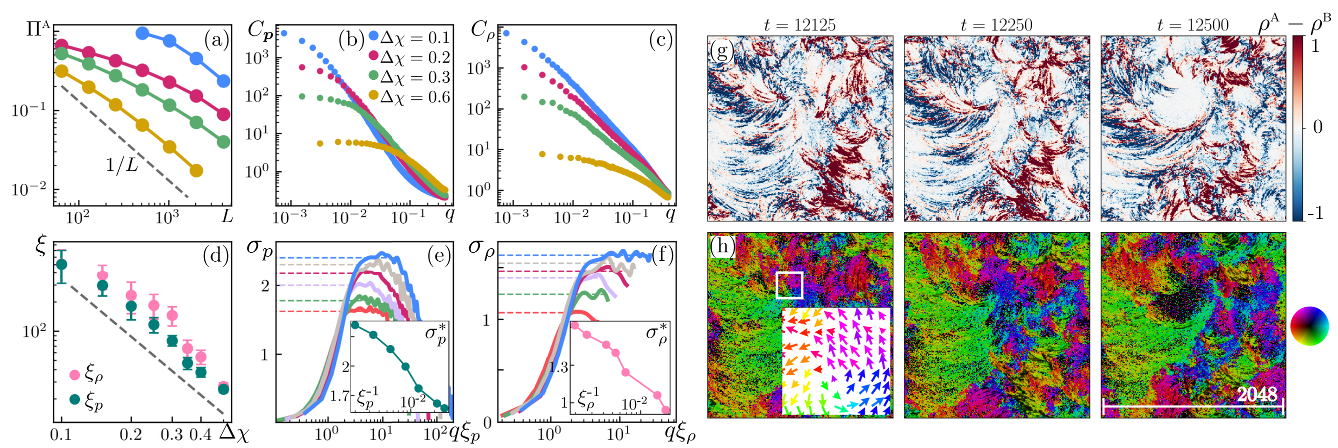

FIG. 2. Characterization of the nonreciprocity-induced defect-chaos phase ($\eta = 0.2$). (a) Time-averaged polar order parameter associated with species A as a function of system size for various values of $\Delta\chi$. (b),(c) Polarity (b) and density fluctuations (c) equal-time correlation function for species A radially averaged over the $(q_x,\ q_y)$ plane as a function of the wave number $q = \sqrt{q_x^2 + q_y^2}$. Legend for (a)–(c) is in (b). (d) Correlation lengths extracted from C_p and C_ρ (see text for details). The dashed line indicates $\xi \simeq \Delta\chi^{-2}$ as a guide to the eye. (e),(f) Local exponent associated with C_p (e) and C_ρ (f) (see text) as a function of $q\xi$ for $\Delta\chi = 0.10,\ 0.15,\ 0.20,\ 0.25,\ 0.30,\ 0.35$, from top to bottom. Insets show the fitted plateau levels (horizontal dashed lines in main panels) as functions of the correlation length. In (b)–(f), system sizes are $L = 8192$ for $\Delta\chi < 0.2$, $L = 4096$ for $0.2 \leq \Delta\chi < 0.4$, and $L = 2048$ otherwise. (g),(h) Snapshots showing the nucleation and growth of a disordered bubble whose diameter at $t = 12\,500$ reaches several hundreds interaction radii for $\Delta\chi = 0.1$. (g) The relative species density and (h) the orientation of the local polarity of A particles, where disordered regions appear black.

show any apparent sign of saturation. The accuracy of our estimates is limited by the finite correlation length, which restricts the range of the scaling regime. Within this limitation, we find effective decay exponents in the range $1.5 \lesssim \sigma_p^* \lesssim 2.5$ and obtain comparable values for species B, while we expect larger values as $\Delta\chi \to 0$.

Density correlations also exhibit intermediate algebraic decay, albeit with smaller exponents. Defining σ_ρ^* from the plateaus associated with the local exponent of $C_\rho(q)$ [Figs. 2(c) and 2(f)], we find that it increases as well when reducing nonreciprocity, and takes values $\sigma_\rho^* \in [1; 1.6]$ similar for both species. Although we cannot, in principle, rule out the existence of a crossover regime, this behavior is incompatible with the compact KPZ scenario. In conventional flocks, the advection of density by self-propulsion, in particular, enforces $C_\rho(q) \propto C_p(q)$, thus fixing $\sigma_p^* = \sigma_\rho^*$ [5,7]. The violation of this relation hence suggests that the presence of strong nonreciprocity qualitatively modifies the large-scale description of the system.

The chiral phase is, however, constantly populated by topological defects, whose dynamics is profoundly affected by the presence of self-propulsion. As illustrated in Figs. 2(g), 2(h) and SMov 3 in Supplemental Material [60], spiral-like defects act as nucleation sites for propagating circular perturbations. Since particles at the core of a vortexlike defect predominantly point outward, once nucleated this structure generates a nearly empty bubble whose radius grows rapidly, leaving an extended dilute and disordered region in place of the original defect. Although the depleted region is eventually refilled by incoming particles, the typical bubble size grows with the correlation length and can reach several hundred interaction ranges for low values of $\Delta\chi$. We naturally expect the continuous generation of such perturbations to significantly affect both density and polarity statistics on scales below the correlation length. We therefore hypothesize that this intrinsically nonlinear mechanism may be responsible for the unconventional scaling behavior reported above.

Continuous description—To elucidate the emergence of the defect chaos state, we derived a continuum theory for nonreciprocal flocks by coarse graining the microscopic model (1). The derivation follows standard techniques [63–65] and generalizes the one performed in Ref. [57] for multispecies flocks without chiral order; details will be presented elsewhere. The resulting theory involves two scalar and two vector fields, corresponding to the coarse-grained densities ρ^{S} and momenta $\boldsymbol{w}^{\mathrm{S}} = \rho^{\mathrm{S}}\boldsymbol{p}^{\mathrm{S}}$ of both species S = A, B. The equations are derived perturbatively close to the ordering threshold, marked by the gray line in Fig. 3(a), as an expansion in gradients and the magnitudes of the momenta. They read (for $i = x$, y and using summation over repeated indices)

$$\partial_t \rho^{\mathrm{S}} + v_0 \nabla \cdot \boldsymbol{w}^{\mathrm{S}} = D_\rho^{\mathrm{S}} \nabla^2 \rho^{\mathrm{S}}, \tag{2a}$$

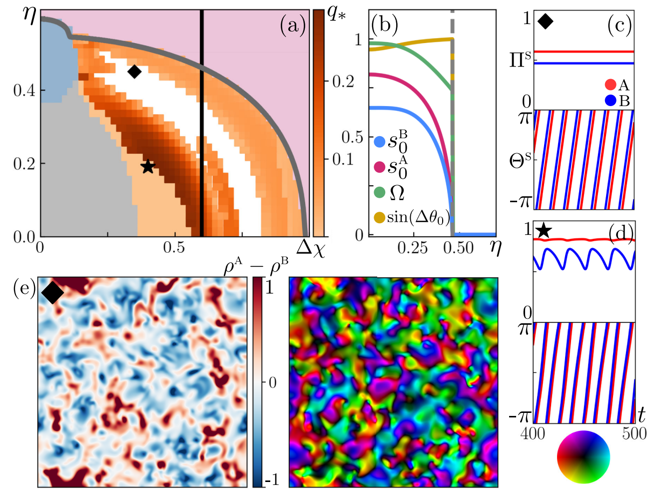

FIG. 3. Phenomenology of the continuum model. (a) Phase diagram showing regions where Eq. (2) admit disordered and homogeneous polar solutions in purple and blue, respectively. Within the orange domain, homogeneous solutions are associated with global chiral order. The color bar indicates the magnitude of the most unstable wave number obtained from Floquet stability analysis, while white indicates that the solution is linearly stable. In the gray region, Eq. (2) exhibit unphysical solutions [66]. (b) Homogeneous uniform chiral solution as a function of the noise η for $\Delta\chi = 0.6$ [black line in (a)]. (c),(d) Time series of the uniform (c) and modulated (d) chiral solutions. Parameters are $(\Delta\chi, \eta) = (0.35, 0.45)$ (c) and (0.4,0.2) (d), marked by the black diamond and star in (a), respectively. (e) Representative simulation snapshots showing the defect-chaos state obtained for the parameters of (c) and $L = 256$ from a random initial condition. The left and right panels show the relative species density and the orientation of the local momentum of A particles (caption on the right), respectively.

$$\begin{aligned}
&\partial_t w_i^{\mathrm{S}} + \psi^{\mathrm{S}}_{\mathrm{UV}}(\boldsymbol{w}^{\mathrm{V}} \cdot \nabla) w_i^{\mathrm{U}} + \lambda^{\mathrm{S}}_{\mathrm{UV}}(\nabla \cdot \boldsymbol{w}^{\mathrm{V}}) w_i^{\mathrm{U}} + \nu^{\mathrm{S}}_{\mathrm{UV}} \boldsymbol{w}^{\mathrm{U}} \cdot \nabla_i \boldsymbol{w}^{\mathrm{V}} \\
&\quad + \tilde{\psi}^{\mathrm{S}}_{\mathrm{UV}}(\boldsymbol{w}^{\mathrm{V}} \cdot \nabla) w^{\mathrm{U}}_{\perp,i} + \tilde{\lambda}^{\mathrm{S}}_{\mathrm{UV}}(\nabla \cdot \boldsymbol{w}^{\mathrm{V}}) w^{\mathrm{U}}_{\perp,i} + \tilde{\nu}^{\mathrm{S}}_{\mathrm{UV}} \boldsymbol{w}^{\mathrm{U}} \cdot \nabla_{\perp,i} \boldsymbol{w}^{\mathrm{V}} \\
&= [\alpha^{\mathrm{S}}_{\mathrm{U}}[\rho^{\mathrm{A}}, \rho^{\mathrm{B}}] - \xi^{\mathrm{S}}_{\mathrm{UVW}}(\boldsymbol{w}^{\mathrm{V}} \cdot \boldsymbol{w}^{\mathrm{W}})] w_i^{\mathrm{U}} - \tilde{\xi}^{\mathrm{S}}_{\mathrm{UVW}}(\boldsymbol{w}^{\mathrm{V}} \cdot \boldsymbol{w}^{\mathrm{W}}) w^{\mathrm{U}}_{\perp,i} \\
&\quad - \frac{v_0}{2} \nabla \rho^{\mathrm{S}} + D^{\mathrm{S}}_{\mathrm{U}} \nabla^2 w_i^{\mathrm{U}} + \tilde{D}^{\mathrm{S}}_{\mathrm{U}} \nabla^2 w^{\mathrm{U}}_{\perp,i},
\end{aligned} \tag{2b}$$

where the subscript $\perp$ denotes vectors rotated by an angle $\pi/2$.

As detailed in [60], coefficients in Eq. (2) depend on the particle-level parameters ρ_0, v_0, η, and χ^{SU} in a complex manner. Compared to continuum theories formulated in related settings [27,43,57], Eq. (2) feature apparent *odd* contributions, including diffusive ($\propto \tilde{D}^{\mathrm{S}}_{\mathrm{U}}$), advective ($\propto \tilde{\psi}^{\mathrm{S}}_{\mathrm{UV}}, \tilde{\lambda}^{\mathrm{S}}_{\mathrm{UV}}, \tilde{\nu}^{\mathrm{S}}_{\mathrm{UV}}$), and effective potential ($\propto \tilde{\xi}^{\mathrm{S}}_{\mathrm{UVW}}$) terms. As required by the chiral symmetry of the microscopic dynamics, which demands that chiral solutions of Eq. (2) must spontaneously break parity symmetry, all tilded coefficients are pseudoscalars and proportional to $\sin(\Delta\theta) = (\boldsymbol{w}^{\mathrm{A}} \times \boldsymbol{w}^{\mathrm{B}})/|\boldsymbol{w}^{\mathrm{A}}||\boldsymbol{w}^{\mathrm{B}}|$. Whenever $\Delta\chi \gg \bar{\chi}$, Eq. (2) indeed admit uniform rotating chiral solutions characterized by homogeneous densities ρ_0^{S} and polar orders $\boldsymbol{w}_0^{\mathrm{S}}(t) = s_0^{\mathrm{S}} \hat{\boldsymbol{u}}(\Omega t + \theta_0^{\mathrm{S}})$ rotating at a uniform frequency Ω and where the two species display a constant phase shift $\Delta\theta_0 = \theta_0^{\mathrm{B}} - \theta_0^{\mathrm{A}}$ [Fig. 3(c)]. Since both Ω and $\sin \Delta\theta_0$ are generally $\mathcal{O}(1)$, they undergo a discontinuous jump at the ordering threshold [Fig. 3(b)], such that the odd terms and their even counterparts in Eq. (2) are effectively of same order in the expansion. When $\Delta\chi$ is sufficiently small, on the other hand, rotating chiral solutions do not exist, $\sin \Delta\theta_0 = 0$, and Eq. (2) reduce to the continuum theory derived in [57]. Setting $\bar{\chi} = 0$, Eq. (2) also admit homogeneous rotating chiral solutions with weak amplitude modulations at low noises [Fig. 3(d)], similar to those reported in Ref. [27]. Finally, for sufficiently low $\Delta\chi$ and high noises chiral solutions are absent and Eq. (2) show homogeneous polar solutions [blue region in Fig. 3(a)] [67].

We performed the Floquet stability analysis of the uniform rotating chiral solution $\rho_0^{\mathrm{S}}, \boldsymbol{w}_0^{\mathrm{S}}(t)$ (details in [60]). As summarized in Fig. 3(a), this solution is unstable for most parameters where it exists, with a linearly stable pocket persisting only at intermediate $\Delta\chi$ [white region in Fig. 3(a)]. Numerical integration of the full nonlinear equations (2) shows that this instability leads to a chaotic regime characterized by the proliferation of topological defects and strong density modulations, reminiscent of active turbulence [68] [Fig. 3(e) and SMov 4 [60]]. Modulated chiral solutions are also unstable, leading to the same outcome. In addition, simulations initialized with random initial conditions in the region where the uniform rotating chiral solution is linearly stable converge again to the defect-chaos state, implying that chiral order is only metastable. These results therefore confirm the scenario evidenced by microscopic simulations: long-range chiral order is generically destroyed by the nucleation and proliferation of topological defects, inducing a finite correlation length.

Discussion—We have shown that, in the strong nonreciprocity regime, multispecies flocks can self-organize into globally polar states through the formation of inhomogeneous traveling band structures. Nevertheless, such systems cannot sustain large-scale chiral order. We demonstrated that chiral order is ultimately destroyed by the proliferation of topological defects, which generate a finite correlation length and cause the rapid decay of global order. These results are further supported by the analysis of a coarse-grained hydrodynamic description, which reveals that chiral solutions are generically unstable or, at best, metastable. In all cases, the dynamics converges to a defect-chaos state dominated by strong spatiotemporal density and polarity fluctuations.

Our numerical simulations further reveal that nonreciprocal flocks exhibit unconventional scaling behavior characterized by nonuniversal exponents, in stark contrast with theoretical expectations based on KPZ roughening, which predict a universal value $\sigma_p^* \simeq 2.8$ [54,69]. We trace this discrepancy to the peculiar role of topological defects, which—through the intrinsic coupling between density and polarity—act as persistent sources of nonlinear fluctuations at scales below the correlation length. Related feedback mechanisms have been discussed in other classes of polar active matter, where they modify the order of phase transitions [70] and affect the coarsening dynamics [71]. Understanding how such density-polarity coupling controls the large-scale behavior of nonreciprocal flocks constitutes an open challenge for future work.

Note added—Recently, two studies appeared that support our conclusion that macroscopic chiral order is destroyed in nonreciprocal flocks [72,73]. Reference [72] reports a generic instability in such systems that leads to large-scale chaotic behavior, while Ref. [73] demonstrates that global chiral motion is sustained only in sufficiently small systems.

Acknowledgments—C. M. acknowledges funding from the International Max Planck Research School (IMPRS) for the Physics of Biological and Complex Systems, and thanks Ramin Golestanian and the Living Matter Department at MPI-DS for supporting her to visit the Charles Coulomb laboratory in Montpellier, and the laboratory for hosting her during part of this work. We thank Irene Pellini for her involvement in the early stages of this work.

Data availability—The data that support the findings of this article are publicly available [74].

[1] N. D. Mermin and H. Wagner, Phys. Rev. Lett. **17**, 1133 (1966).
[2] P. C. Hohenberg, Phys. Rev. **158**, 383 (1967).
[3] T. Vicsek, A. Czirók, E. Ben-Jacob, I. Cohen, and O. Shochet, Phys. Rev. Lett. **75**, 1226 (1995).
[4] J. Toner and Y. Tu, Phys. Rev. Lett. **75**, 4326 (1995).
[5] J. Toner and Y. Tu, Phys. Rev. E **58**, 4828 (1998).
[6] J. Toner, Phys. Rev. E **86**, 031918 (2012).
[7] B. Mahault, F. Ginelli, and H. Chaté, Phys. Rev. Lett. **123**, 218001 (2019).
[8] H. Chaté and A. Solon, Phys. Rev. Lett. **132**, 268302 (2024).
[9] P. Jentsch and C. F. Lee, Phys. Rev. Lett. **133**, 128301 (2024).
[10] L. Chen, P. Jentsch, C. F. Lee, A. Maitra, S. Ramaswamy, and J. Toner, arXiv:2503.17064.
[11] F. Ginelli, F. Peruani, M. Bär, and H. Chaté, Phys. Rev. Lett. **104**, 184502 (2010).
[12] B. Mahault and H. Chaté, Phys. Rev. Lett. **127**, 048003 (2021).
[13] L. P. Dadhichi, J. Kethapelli, R. Chajwa, S. Ramaswamy, and A. Maitra, Phys. Rev. E **101**, 052601 (2020).

[14] S. A. M. Loos, S. H. L. Klapp, and T. Martynec, Phys. Rev. Lett. **130**, 198301 (2023).
[15] D. Dopierala, H. Chaté, X.-q. Shi, and A. Solon, Phys. Rev. Lett. **135**, 088302 (2025).
[16] G. Pisegna, S. Saha, and R. Golestanian, Proc. Natl. Acad. Sci. U.S.A. **121**, e2407705121 (2024).
[17] Y.-E. Keta and S. Henkes, Soft Matter **21**, 5710 (2025).
[18] J. Codina, B. Mahault, H. Chaté, J. Dobnikar, I. Pagonabarraga, and X.-q. Shi, Phys. Rev. Lett. **128**, 218001 (2022).
[19] M. Besse, H. Chaté, and A. Solon, Phys. Rev. Lett. **129**, 268003 (2022).
[20] B. Benvegnen, O. Granek, S. Ro, R. Yaacoby, H. Chaté, Y. Kafri, D. Mukamel, A. Solon, and J. Tailleur, Phys. Rev. Lett. **131**, 218301 (2023).
[21] C.-U. Woo and J. D. Noh, Phys. Rev. Lett. **133**, 188301 (2024).
[22] P. Popli, A. Maitra, and S. Ramaswamy, Phys. Rev. Lett. **135**, 088303 (2025).
[23] M. J. Bowick, N. Fakhri, M. C. Marchetti, and S. Ramaswamy, Phys. Rev. X **12**, 010501 (2022).
[24] M. Fruchart and V. Vitelli, arXiv:2602.11111.
[25] S. Saha, J. Agudo-Canalejo, and R. Golestanian, Phys. Rev. X **10**, 041009 (2020).
[26] Z. You, A. Baskaran, and M. C. Marchetti, Proc. Natl. Acad. Sci. U.S.A. **117**, 19767 (2020).
[27] M. Fruchart, R. Hanai, P. B. Littlewood, and V. Vitelli, Nature (London) **592**, 363 (2021).
[28] J. Agudo-Canalejo and R. Golestanian, Phys. Rev. Lett. **123**, 018101 (2019).
[29] T. Frohoff-Hülsmann, J. Wrembel, and U. Thiele, Phys. Rev. E **103**, 042602 (2021).
[30] Y. Duan, J. Agudo-Canalejo, R. Golestanian, and B. Mahault, Phys. Rev. Lett. **131**, 148301 (2023).
[31] A. Dinelli, J. O'Byrne, A. Curatolo, Y. Zhao, P. Sollich, and J. Tailleur, Nat. Commun. **14**, 7035 (2023).
[32] F. Brauns and M. C. Marchetti, Phys. Rev. X **14**, 021014 (2024).
[33] N. Rana and R. Golestanian, Phys. Rev. Lett. **133**, 078301 (2024).
[34] Y. Duan, J. Agudo-Canalejo, R. Golestanian, and B. Mahault, Phys. Rev. Res. **7**, 013234 (2025).
[35] D. Greve, G. Lovato, T. Frohoff-Hülsmann, and U. Thiele, Phys. Rev. Lett. **134**, 018303 (2025).
[36] S. Saha and R. Golestanian, Nat. Commun. **16**, 7310 (2025).
[37] R. Hanai, Phys. Rev. X **14**, 011029 (2024).
[38] K. L. Kreienkamp and S. H. L. Klapp, Phys. Rev. Lett. **133**, 258303 (2024).
[39] K. L. Kreienkamp and S. H. L. Klapp, Phys. Rev. E **110**, 064135 (2024).
[40] L. Guislain and E. Bertin, Phys. Rev. E **109**, 034131 (2024).
[41] L. Guislain and E. Bertin, J. Stat. Mech. (2024) P093210.
[42] J. Chen, X. Lei, Y. Xiang, M. Duan, X. Peng, and H. P. Zhang, Phys. Rev. Lett. **132**, 118301 (2024).
[43] K. L. Kreienkamp and S. H. L. Klapp, Commun. Phys. **8**, 307 (2025).
[44] Y. Avni, M. Fruchart, D. Martin, D. Seara, and V. Vitelli, Phys. Rev. Lett. **134**, 117103 (2025).
[45] Y. Avni, M. Fruchart, D. Martin, D. Seara, and V. Vitelli, Phys. Rev. E **111**, 034124 (2025).
[46] M. Mangeat, S. Chatterjee, J. D. Noh, and H. Rieger, Commun. Phys. **8**, 186 (2025).
[47] D. Martin, D. Seara, Y. Avni, M. Fruchart, and V. Vitelli, Phys. Rev. X **15**, 041015 (2025).
[48] K. Blom, U. Thiele, and A. Godec, Phys. Rev. E **111**, 024207 (2025).
[49] M. Kardar, G. Parisi, and Y.-C. Zhang, Phys. Rev. Lett. **56**, 889 (1986).
[50] G. Grinstein, D. Mukamel, R. Seidin, and C. H. Bennett, Phys. Rev. Lett. **70**, 3607 (1993).
[51] H. Chaté, G. Grinstein, and L.-H. Tang, Phys. Rev. Lett. **74**, 912 (1995).
[52] A. Maitra, Annu. Rev. Condens. Matter Phys. **16**, 275 (2025).
[53] R. Daviet, C. P. Zelle, A. Asadollahi, and S. Diehl, Phys. Rev. Lett. **135**, 047101 (2025).
[54] L. Canet, H. Chaté, B. Delamotte, and N. Wschebor, Phys. Rev. Lett. **104**, 150601 (2010).
[55] G. Wachtel, L. M. Sieberer, S. Diehl, and E. Altman, Phys. Rev. B **94**, 104520 (2016).
[56] K. Deligiannis, Q. Fontaine, D. Squizzato, M. Richard, S. Ravets, J. Bloch, A. Minguzzi, and L. Canet, Phys. Rev. Res. **4**, 043207 (2022).
[57] C. Myin and B. Mahault, Phys. Rev. Lett. **137**, 018301 (2026).
[58] H. Chaté, Annu. Rev. Condens. Matter Phys. **11**, 189 (2020).
[59] A. Maitra, M. Lenz, and R. Voituriez, Phys. Rev. Lett. **125**, 238005 (2020).
[60] See Supplemental Material at http://link.aps.org/supplemental/10.1103/c6dy-38z1 for further details on numerical protocols regarding the construction of the phase diagram of Fig. 1 and the resolution of the continuum model, as well as a description of the accompanying movies, which also includes Ref. [61].
[61] G. E. Santoro, Introduction to Floquet (2019).
[62] For $\bar{\chi} = 0$, the two species never form a homogeneous ordered phase. For $\bar{\chi} > 0$ and $\bar{\chi} < 0$, polar and antipolar homogeneous ordered phases, respectively, may be found at sufficiently small $\Delta\chi$, see supplement.
[63] E. Bertin, M. Droz, and G. Grégoire, Phys. Rev. E **74**, 022101 (2006).
[64] A. Peshkov, E. Bertin, F. Ginelli, and H. Chaté, Eur. Phys. J. Special Topics **223**, 1315 (2014).
[65] H. Chaté and B. Mahault, in *Active Matter and Non-equilibrium Statistical Physics: Lecture Notes of the Les Houches Summer School: Volume 112, September 2018* (Oxford University Press, New York, 2022).
[66] In the gray region, located far from the ordering threshold, the assumption of small global order underlying the derivation of the continuum model is not verified.
[67] Polar solutions of Eq. (2) are generally unstable.
[68] R. Alert, J. Casademunt, and J.-F. Joanny, Annu. Rev. Condens. Matter Phys. **13**, 143 (2022).
[69] T. Kloss, L. Canet, and N. Wschebor, Phys. Rev. E **86**, 051124 (2012).

[70] B. Mahault, X.-c. Jiang, E. Bertin, Y.-q. Ma, A. Patelli, X.-q. Shi, and H. Chaté, Phys. Rev. Lett. **120**, 258002 (2018).

[71] A. Chardac, L. A. Hoffmann, Y. Poupart, L. Giomi, and D. Bartolo, Phys. Rev. X **11**, 031069 (2021).

[72] C.-U. Woo, J. D. Noh, and H. Rieger, preceding Letter, Phys. Rev. Lett. **137**, 118301 (2026).

[73] A. K. Dutta, S. Chatterjee, M. Mangeat, and R. Paul, arXiv:2604.18125.

[74] C. Myin, Data for Breakdown of emergent Chiral order and defect chaos in nonreciprocal flocks (2026), 10.17617/3.NXLSEM.

End Matter

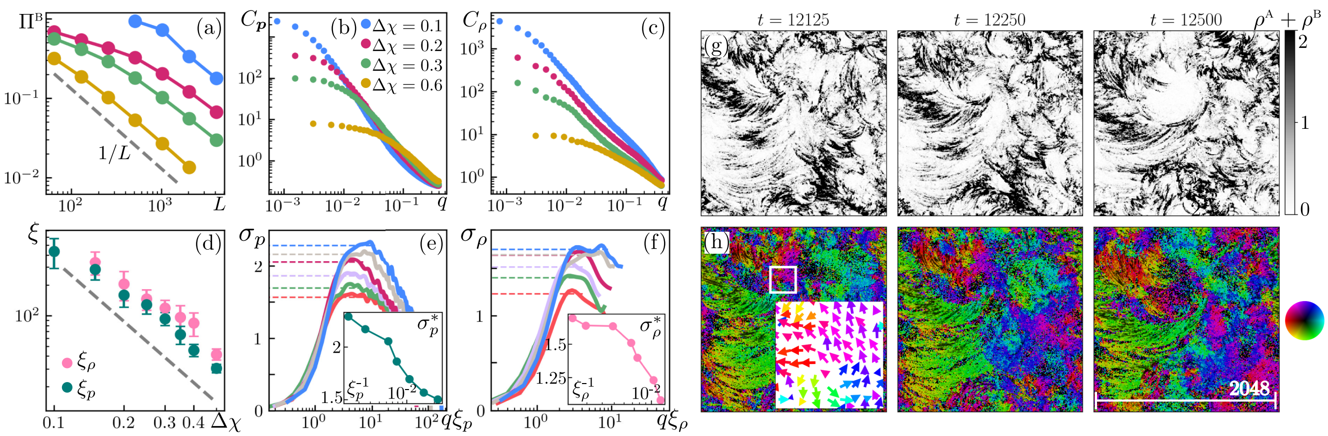

FIG. 4. This figure corresponds to Fig. 2 of the main text, but with global order, correlation functions, and correlation length extracted from species B with $\eta = 0.2$. (a) Time-averaged polar order parameter associated with species B as a function of system size for various values of $\Delta\chi$. (b),(c) Polarity (b) and density fluctuations (c) equal-time correlation function for species B radially averaged over the (q_x, q_y) plane as a function of the wave number $q = \sqrt{q_x^2 + q_y^2}$. Legend for (a)–(c) is in (b). (d) Correlation lengths extracted from C_p and C_ρ (see main text for details). The dashed line indicates $\xi \simeq \Delta\chi^{-2}$ as a guide to the eye. (e),(f) Local exponent associated with C_p (e) and C_ρ (f) (see text) as a function of $q\xi$ for $\Delta\chi = 0.10, 0.15, 0.20, 0.25, 0.30, 0.35$, from top to bottom. Insets show the fitted plateau levels (horizontal dashed lines in main panels) as functions of the correlation length. In (b)–(f), system sizes are $L = 8192$ for $\Delta\chi < 0.2$, $L = 4096$ for $0.2 \leq \Delta\chi < 0.4$, and $L = 2048$ otherwise. (g),(h) Snapshots showing the nucleation and growth of a disordered bubble whose diameter at $t = 12\,500$ reaches several hundreds interaction radii for $\Delta\chi = 0.1$. (g) The total species density and (h) the orientation of the local polarity of B particles, where disordered regions appear black.